Texture-Sensitive Superpixeling and Adaptive Thresholding for Effective Segmentation of Sea Ice Floes in High-Resolution Optical Images

Yanmei Chai, Jinchang Ren, *Senior Member, IEEE*, Byongjun Hwang, *Member, IEEE*, Jian Wang, Dan Fan, Yijun Yan, and Shiwei Zhu

***Abstract*—Efficient and accurate segmentation of sea ice floes from high-resolution optical (HRO) remote sensing images is crucial for understanding of sea ice evolutions and climate changes, especially in coping with the large data volume. Existing methods suffer from noise interference and the mixture of water and ice caused high segmentation error and less robustness. In this article, we propose a novel sea ice floe segmentation algorithm from HRO images based on texture-sensitive superpixeling and two-stage thresholding. First, sparse components are extracted from the HRO images using the robust principal component analysis (RPCA), and noise is removed by the bilateral filter. The enhanced image is obtained by combining the low-rank matrix and the sparse components. Second, a texture-sensitive simple linear iterative clustering (SLIC) superpixel algorithm is introduced for presegmentation of the enhanced HRO image. Third, a learning-based adaptive thresholding in the two stages is employed to generate the refined segmentation from the derived superpixels blocks. The efficacy of the proposed method is validated on two HRO images using visual assessment, quantitative evaluation (with seven metrics), and histogram comparison. The superior performance of the proposed method has demonstrated its efficacy for sea ice floe segmentation.**

***Index Terms*—Adaptive two-stage thresholding, high-resolution optical (HRO) image, low-rank sparse representation, sea ice floe segmentation, texture-sensitive superpixeling.**

I. Introduction

SEA ice floe segmentation is an important topic in remote sensing. It is essential for understanding the climate and environmental change and for safe navigation of ships in waters where sea ice forms [1]. With regular data provided covering, an increasingly wide area, and a relatively high temporal resolution, various satelliteborne sensors are used in sea ice applications. However, each sensor has certain strengths and weaknesses. For example, although scatterometers can provide a fast and noncontact method for topography assessment, it suffers from a low spatial resolution and, hence, can only detect large sea ice floes or icebergs. For deformed sea ices, radar altimeters are also restricted. As the synthetic aperture radar (SAR) acquires data at all time in any weather conditions, it is widely used for sea ice analysis [2]. However, SAR suffers from severe speckle noise and limited spatial resolution; hence, it is difficult to detect small ice floes [3]. In addition, collecting data from observational aircraft is difficult and expensive. With the advancement of satellite technology, high-resolution optical (HRO) imagery has provided another alternative solution, as it enables accurate detection of the textures, shapes, and edges of the sea ice floes [4].

In order to precisely segment water–ice from HRO images, many studies have been done. Early attempts include grey level co-occurrence probability texture features [5], function-based Markov random field model algorithm [6], and *k*-means clustering [7]. In addition, region-based segmentation is also focused, which include watershed and iterative region growing with semantics [8], incidence angle effect correction and region merging [1], and watershed with intensity-based region merging method [9]. In general, good segmentation results can be produced if the contrast between the sea ice and its surrounding background is sufficiently high; thus, it fails to deal with cases of mixed melting ice and water as the contrast becomes quite low.

Due to the complicated dynamics of the sea ice under the changing environmental effects such as wind, temperature, and ocean current, it is extremely difficult to model and detect small sea ice floes. At present, most of the sea ice image segmentation methods are for SAR images. In [10], deep learning approach is also attempted for classification of ocean surface in SAR images. However, due to the lack of sufficient samples and labeled data the application is very limited, whereas the few shot learning is difficult to meet the needs, especially sea ice floe segmentation. Although high-resolution optical images can visually capture the surface features of interest, relevant approaches for sea ice floe segmentation remain under-developed and distance

Manuscript received June 30, 2020; revised October 19, 2020 and November 17, 2020; accepted November 23, 2020. Date of publication November 25, 2020; date of current version January 6, 2021. This work was supported in part by the Natural and Environmental Research Council under Grant NE/S002545/1, U.K., in part by the Visiting Scholarship funded by the China Scholarship Council under Grant 201906495007, in part by the Dazhi Scholarship of the Guangdong Polytechnic Normal University, National Natural Science Foundation of China under Grant 62072122, and in part by the Education Department of Guangdong Province under Grant 2019KSYS009. *(Corresponding author: Jinchang Ren.)*

Yanmei Chai, Jian Wang, Dan Fan, and Shiwei Zhu are with the School of Information, Central University of Finance and Economics, Beijing 100081, China (e-mail: ymchai@cufe.edu.cn; wangjian-cufe@cufe.edu.cn; fandan@cufe.edu.cn; zhusw@cufe.edu.cn).

Jinchang Ren is with the National Subsea Centre, Robert Gordon University, Aberdeen, U.K., and also with the Guangdong Polytechnic Normal University, Guangzhou 510665, China (e-mail: jinchang.ren@ieee.org).

Yijun Yan is with the Department of Electronic and Electrical Engineering, University of Strathclyde, G1 1XW Glasgow, U.K. (e-mail: yijun.yan@strath.ac.uk).

Byongjun Hwang is with the Department of Biological and Geographical Sciences, University of Huddersfield, HD1 3DH Huddersfield, U.K. (e-mail: b.hwang@hud.ac.uk).

Digital Object Identifier 10.1109/JSTARS.2020.3040614

away from practical needs. In addition to thresholding [11] and watershed-based segmentation [12], there has been growing interest recently in pixel grouping, i.e., object-based segmentation. The object-based segmentation was particularly useful for sea ice floe segmentation, where each floe can be treated as one individual object. Neighboring pixels can be grouped into objects according to the similarity of their intensity and textural features [13]. However, due to the difficulty in defining object boundaries in sea ice images, superpixel-based segmentation is preferred as it provides an intermediate level representation between pixels and objects.

Recently, superpixel segmentation has been applied for object detection or image segmentation in remote sensing images. These include superpixel graph-based segmentation algorithm with ensemble learning and incremental learning [14] and combining superpixels with the minimum spanning tree [15]. However, these methods are not aimed at sea ice segmentation from high-resolution optical images. As a result, we aim to apply superpixel for sea ice floe segmentation from HRO images, where the challenges are how to deal with the low contrast areas of mixed ice and water and also accurate segmentation of touching floes of arbitrary sizes and shapes. Meanwhile, efficient implementation is needed to cope with the pressure of large data volume in the context of big data analysis.

By grouping spatially adjacent similar pixels into small regions, superpixel segmentation can significantly simplify the computational efficiency and improve the efficacy of following-on analysis. This is particularly useful for sea ice image segmentation, as the images are often very large in size and the pixels for either the water background or sea ice floes have quite similar appearance. The only exception is the mixture of water and ice pixels, i.e., regions of melting ices. As a result, texture sensitive superpixeling is proposed to tackle this challenge.

The major contributions of the proposed approach can be highlighted as follows: First, we apply the robust principal component analysis (RPCA) and low-rank representation for denoising of the input images. Second, we combine texture sensitive superpixeling and a learning-based adaptive thresholding for efficient and effective segmentation of sea ice floes. Both visual and quantitative assessments have validated the superior performance of the proposed approach in denoising and accurate segmentation of sea ice floes in comparison to the state-of-the-art approaches.

The remaining parts of this article are organized as follows. Section II presented the proposed algorithm in detail, with the experimental settings detailed in Section III. The experimental results are summarized and discussed in Section IV. Finally, Section V concludes this article.

II. Proposed Methodology

In Fig. 1, the flowchart of the proposed approach is illustrated. First, sparse components are extracted from the high-resolution remote sensing image by using RPCA, and the bilateral filter is used on it to remove noise. The enhanced image is obtained by combining the low-rank matrix and the sparse components. Second, applying the proposed texture-sensitive superpixeling algorithm to presegment the enhanced high-resolution optical image. Finally, these superpixels are then processed using the two-stage thresholding to generate the final segmentation. The whole processing is divided into denoising and segmentation. In simple linear iterative clustering (SLIC), the k-means clustering approach is adopted to generate superpixels [16]. For determining the nearest cluster center for each image pixel, both the color and spatial features are used to measure the distance D. In fact, in HRO images, the roughness degree of different ocean cover surfaces brings about different texture properties. The employed textural information can help to exploit the underlying spatial information so that the accuracy (ACC) of classification can be improved [17]. As a result, we have introduced the texture feature into the distance measure D for better segmentation of sea ice floes. These superpixels are then processed using a two-stage thresholding to generate the final segmentation as detailed below.

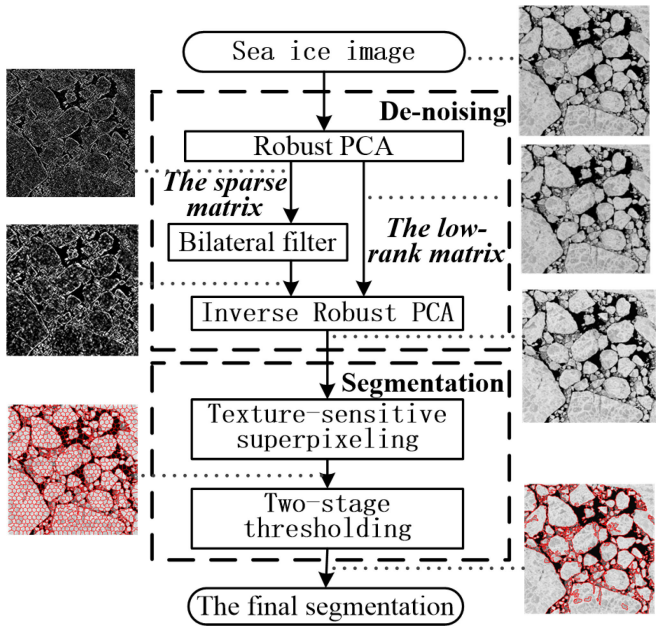

Fig. 1. Flowchart of proposed algorithm for sea ice floe segmentation.

A. De-Noising Using the RPCA

Due to the effect of illumination changes, atmosphere effect, and sensor noise, remote sensing images often suffer from different kinds of noise, which may appear in Gaussian, stripe, impulse, spectral, speckle, temporal, or mixed patterns. Such noise may severely degrade the image quality and constraint the performance of the subsequent processing, e.g., segmentation of small ice floes. By experimental analysis, it is found that the major noise in our tested images are mixed patterns. Conventional filtering approaches are found to fail in such cases, as they may selectively smooth some noisy parts of the image whilst blur details in other parts. In fact, as remote sensing images are characterized with low-rankness, i.e., sparsity, which means that the high-dimensional data can be adequately represented in a low-dimensional subspace for dimensionality reduction [31].

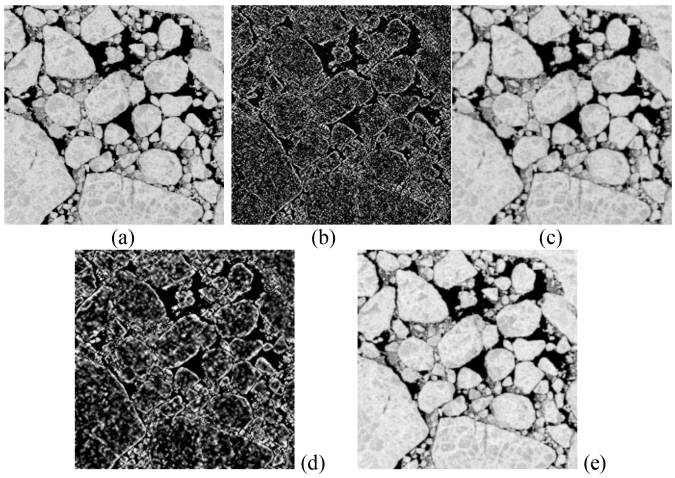

Fig. 2. Sample output of the noise reduction processing. (a) Original image. (b) Sparse matrix. (c) Low-rank matrix. (d) Filtered sparse matrix using bilateral filter. (e) Enhanced image.

Basically, the noise component tends to be sparse and lies in the sparse subspace on the dataset. Thus, the remote sensing images can be transformed into a sparse matrix and a low-rank matrix, which can be solved by using a computational tool namely RPCA [19].

Let $\mathrm{Y} \in R^{m\times n}$ be the input data, RPCA can be regarded as a convex optimization problem and described as follows:

$$\min_{L,E} \|L\|_* + \lambda\|E\|_1 \ \text{s.t.}\ Y = L + E \tag{1}$$

where $\mathrm{L} \in R^{m\times n}$ and $\mathrm{E} \in R^{m\times n}$ denote, respectively, the low-rank component and the sparse component; $\|L\|_* = \sum_r \delta_r(L)$ is the nuclear norm of *L*, whose $r\mathrm{th}$ singular value is denoted as $\delta_r(L)(r = 1, 2, \ldots, \min(m, n))$; $\|E\|_1 = \sum_{ij} |e_{ij}|$ is the L_1-norm, and e_{ij} is the element at the $i\mathrm{th}$ row and $j\mathrm{th}$ column. *L* and *E* can exactly recover *Y* with a high probability under certain rank upper-bound and noise sparsity assumptions [18]. The optimization method used is the alternating direction method of multipliers (ADMM) algorithm [20].

Following the decomposing of RPCA, we apply the bilateral filter to remove noise in the sparse matrix. As a nonlinear filter, it can smooth the image and reduce noise without blurring the edges, as detailed in [21]. At last, the image can be restored by combining the low-rank component and the de-noised sparse component.

Fig. 2 shows the results of noise reduction from RPCA on an example image. The 512×512 sample image was taken from a HRO image in the Arctic (Chukchi Sea [22]). As seen, Fig. 2(d) is better than Fig. 2(b) from visual comparison. The RPCA-based method and bilateral filter have effectively removed most of the noise from the sparse matrix while clearly maintaining the boundary of the sea ice floes.

In Table I, the mean-squared error (MSE) and signal noise ratio (SNR) are used for quantitative evaluation of the de-noising effect. As seen, our method using RPCA and bilateral filter has improved the MSE and SNR than median filtering, Wiener filtering, and the case with only the bilateral filtering.

TABLE I
QUANTITATIVE EVALUATION OF DE-NOISING

Method	MSE	SNR
Original image	65.30	2.30
Original image + Wiener filter	63.84	2.35
Original image + median filter	64.57	2.33
Original image +bilateral filter	65.09	2.31
Original image + RPCA+ bilateral filter	68.27	2.46

B. Texture-Sensitive Superpixeling-Based Segmentation

As superpixels have been successfully applied in other image segmentation tasks [14], [15], we use it in our problem for segmenting individual sea ice floes, especially the small floes, for efficient analysis of the large HRO images. By grouping pixels into meaningful patches, superpixels can significantly reduce the complexity of following-on tasks of image analysis [16]. Among quite a few superpixeling algorithms, SLIC is used for its simple, fast, and more memory efficient implementation and better adherence to image boundaries [16].

The general SLIC works like as follows. First, the number of superpixels *K* is specified, and each superpixel will have approximately *N/K* pixels, and the interval between their centroids is $S = \sqrt{N/K}$, where *N* is the total number of image pixels. Denote the cluster centers of the *K* selected superpixels as $C_k = [l_k,\ a_k, b_k, x_k, y_k]$ with $k \in \{1, \ldots, K\}$ at a regular grid interval *S*. The cluster centers are represented using a 5-D vector, which contains the spatial coordinate (*x*,*y*) and three color components (*L*,*a*,*b*) derived from the CIELAB colorspace.

For two pixels *i* and *j*, their color, spatial, and combined distances d_c, d_s, and D, can be measured using the Euclidean distance as follows:

$$d_c = \sqrt{(l_i - l_j)^2 + (a_i - a_j)^2 + (b_i - b_j)^2} \tag{2}$$

$$d_s = \sqrt{(x_i - x_j)^2 + (y_i - y_j)^2}. \tag{3}$$

$$D = \sqrt{{d_c}^2 + \left(m\frac{d_s}{S}\right)^2} \tag{4}$$

where *m* is a parameter to control the spatial compactness of the superpixels. A larger *m* emphasizes more the spatial proximity and, hence, a more compact cluster. The value of *m* varies within [1] and [20], and its default value is set to 10 [16].

In the conventional SLIC approach, only the color and spatial coordinates are utilized for generating the superpixels. Due to similar intensity and lack of shape and other constraints, texture features are extremely important for sea ice floes in the HRO images, especially for detecting small sea ice floes in the mixture of ice and water. For simplicity, the texture descriptor is also extracted from local image blocks, using the local directional ZigZag pattern (LDZP) as it has superior texture representation capability than a few existing approaches, such as local binary pattern, local ternary pattern, and local derivative pattern [23].

Using the LDZP [23], a texture descriptor can be extracted for each pixel in a 3×3 local window. For two pixels i and j, denote LDZP_i and LDZP_j as the corresponding LDZP-based texture descriptors. Their distance can also be measured using

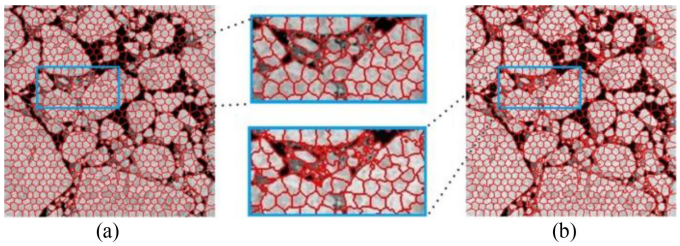

Fig. 3. (a) Superpixels generated by SLIC. (b) Texture-sensitive SLIC.

the Euclidean distance below as follows:

$$d_t = \sqrt{\sum_{n=1}^{N} (\mathrm{LDZP}_{i,n} - \mathrm{LDZP}_{j,n})^2} \tag{5}$$

where n is the index of the N neighbors in the local window, and we have $N = 8$ for a 3×3 local window.

The distance D in (4) is then further updated to include the texture-features as follows:

$$D = \sqrt{{d_c}^2 + \left(\frac{d_s}{S}\right)^2 m^2 + {d_t}^2}. \tag{6}$$

In Fig. 3, we compare the superpixels generated by SLIC and our refined texture-sensitive SLIC. As seen, the proposed texture-sensitive SLIC is able to retain more detailed texture information with clearer boundary. This has the great potential to extract small ice floes as verified in the following section.

C. Refined Segmentation Using Two-Stage Thresholding

By analyzing the superpixels pictures generated by SLIC and texture-sensitive SLIC, we find that most of superpixels blocks adhere the boundary well. While there are still some blocks which contain both the ice and water, especially in areas of melting ice in the open water. In other words, some superpixels blocks are under-segmented. For improved segmentation, two-stage thresholding is proposed to further process these superpixels blocks.

Through the analysis of the image histogram, it is found that the original images are usually obvious bimodal distribution. Therefore, the bottom of the valley can be used as the segmentation threshold T. The variance V of the original image is computed and $T + V$ and $T - V$ can be used as the thresholds of the first layer segmentation, respectively. Furthermore, the mean μ is computed for each superpixels block and the superpixels block can be considered as sea ices if the μ is more than $T + V$. Otherwise, the superpixels block can be considered as sea water if the μ is less than $T - V$. For superpixels blocks whose μ values are between $T - V$ and $T + V$, they are considered as the mixture of ice and water and will be further segmented.

For the mixed ice–water blocks, the second segmentation stage is needed. First, the mean u and the variance v are computed and the threshold $u + \omega * v$ is obtained, in which ω is an adjustment factor. The mixed ice–water blocks are segmented by comparing each pixel value against the threshold.

The key parameter ω is actually adaptively determined by using the support vector machine (SVM), where we select 50% of the regions for training and the remaining for testing. For training, we manually determine the best ω for each mixed ice–water block, and followed by support vector regression analysis to derive the ω automatically for the testing blocks. The LibSVM was used for implementing the SVM [24]. Finally, the two-stage thresholding algorithm can be described using the following pseudocode:

```
T ← threshold of bimodal segmentation of the original
 image
V ←variance of the original image
For each superpixels block
  μ ←mean of each superpixels block
  v ←variance of each superpixels block
  If μ > = T+V
    Superpixels block is sea ice
  Elseif μ < = T − V
    Superpixels block is sea water
  Else
    Determine the optimal threshold ω using SVM
    For each pixel in superpixels block
      If Grayscale > = u + ω ∗ v
        The pixel is sea ice
      Else
        The pixel is sea water
      End
    End
End
```

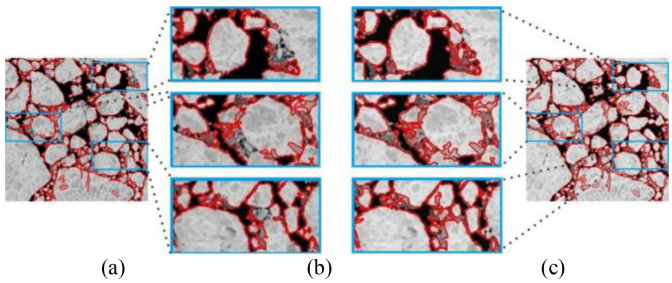

Fig. 4. Label outputs segmented by two-stage thresholding method. (a) Label output from the original SLIC algorithm. (b) Enlarged details comparison. (c) Label output from our texture-sensitive SLIC algorithm.

Fig. 4(a)–(c) shows the label outputs segmented by using the two-stage thresholding on results of the SLIC superpixels and texture-sensitive SLIC, respectively. On the whole, both methods can segment large chunks of ice well. However, by examining the details as highlighted in the label outputs, we can see that some small ice floes in the ice–water mixing area are missed by the general SLIC algorithm. In fact, obtaining small ice floes is important for the subsequent processing and analysis of sea ice melting [25]. To this end, the proposed texture-sensitive SLIC algorithm seems to obtain improved segmentation with fine detail.

III. Experimental Settings

A. Image Dataset

In 2009, the U.S. Geological Survey (USGS) released to the public numerous HRO images acquired since 1999 at six locations in the Arctic Basin (i.e., Canadian Arctic, Chukchi Sea, Beaufort Sea, Fram Strait, East Siberian Sea, and Point Barrow) for studying of shifts in Arctic Ocean sea ice cover and understanding the environmental changes. With a spatial resolution of 1 m, each geocoded panchromatic image covers an area of approximately 15 × 15 km of the Arctic sea ice. In addition, in order to obtain a single cloud-free scene of the surface, repeated acquisitions are typically required since Arctic stratus clouds frequently obstruct imaging of the surface during the summer [26]. In this study, two HRO images from the Global Fiducials Library (GFL) [22] are used to verify the proposed algorithm. The Chukchi Sea and East Siberian Sea images were, respectively, acquired on 31 May 2013 and 16 June 2001. The data type of both images is unsigned 8-bit integer.

B. Ground Truth (GT) and Evaluation Metrics

For evaluation of the segmentation results, the most intuitive method is visual comparison. Considering the large size of the images and the massive volume of the data, however, it is unrealistic to evaluate the segmentation results by visual comparison in this context. For the sake of quantitative performance evaluation, a GT image is needed for quantitative evaluation. Due to the dynamic nature of the scene and the ambiguous boundaries between the water and ice during melting, it is a very challenging or even impossible task to obtain an error-free GT, even by domain experts in a manual way. Despite of such difficulties, manual analysis has been widely adopted for analyzing sea ice images [27].

In this study, manual GT is also used for the test image of the Chukchi Sea [22]. A region of interest of 6368 × 2584 pixels is cropped from the original image for simplicity. The GT data were produced by combining software and manual analysis, where an initial segmentation from the environment for visualizing images (ENVI) is further manually corrected by an experienced sea ice expert to generate the corresponding GT.

The following popularly used metrics are adopted for quantitative evaluation of the segmentation results, including the ACC, Precision, Recall, F_1-measure, Jaccard coefficient (JAC), Matthews Correlation Coefficient (MCC), and Conformity [28]. All these metrics can be derived from the confusion matrix, using several statistical measures such as the numbers of true positives (TP), false positives (FP), true negatives (TN), and false negatives (FN). Their definitions are briefly summarized as follows:

$$\text{Accuracy} = \frac{\text{TP} + \text{TN}}{\text{TP} + \text{TN} + \text{FP} + \text{FN}} \tag{7}$$

$$\text{Precision} = \frac{\text{TP}}{\text{TP} + \text{FP}} \tag{8}$$

$$\text{Recall} = \frac{\text{TP}}{\text{TP} + \text{FN}}. \tag{9}$$

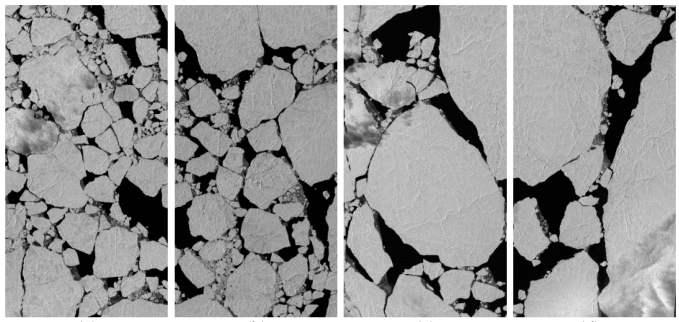

Fig. 5. Original HRO image divided into four subimages. (a) Top-left. (b) Top-right. (c) Bottom-left. (d) Bottom-right.

As the Precision and Recall values are in conflict, a combined metric F_β-measure is defined as follows:

$$F_\beta = \frac{\left(\beta^2 + 1\right) \text{Precision} * \text{Recall}}{\beta^2 \text{Precision} + \text{Recall}}. \tag{10}$$

When $\beta = 1$, the widely used F_1-measure can be derived as follows:

$$F_1 = \frac{2\text{TP}}{2\text{TP} + \text{FP} + \text{FN}}. \tag{11}$$

The JAC defined by the following:

$$\text{Jaccard} = \frac{\text{TP}}{\text{TP} + \text{FP} + \text{FN}}. \tag{12}$$

The MCC is defined as follows:

$$\text{MCC} = \frac{\text{TP} * \text{TN} - \text{FP} * \text{FN}}{\sqrt{(\text{TP} + \text{FP})\,(\text{TP} + \text{FN})\,(\text{TN} + \text{FP})\,(\text{TN} + \text{FN})}}. \tag{13}$$

The Conformity below is a coefficient for characterizing the global error of the segmentation [26].

$$\text{Conformity} = 1 - \frac{\text{FP} + \text{FN}}{\text{TP}}. \tag{14}$$

IV. Results and Validation

A. Visual Comparison

For the East Siberian Sea image [22], it has a spatial size of 3684 × 7056 pixels. For performance evaluation of the proposed approach, the image is equally divided into four subimages (see in Fig. 5), where each subimage has a size of 1842 × 3529 pixels. The sea ice segmentation based on general SLIC and texture-sensitive SLIC are carried on them, respectively.

Fig. 6 shows the visual comparison of segmentation results. The left column shows the label output from the original SLIC algorithm, the right column shows the label output from our texture-sensitive SLIC algorithm, and the middle columns show the enlarged details comparisons. As seen, both methods can well segment large sea ice floes. However, the proposed method performs significantly better in segmenting small ice floes as highlighted in the close-up views of the selected image blocks.

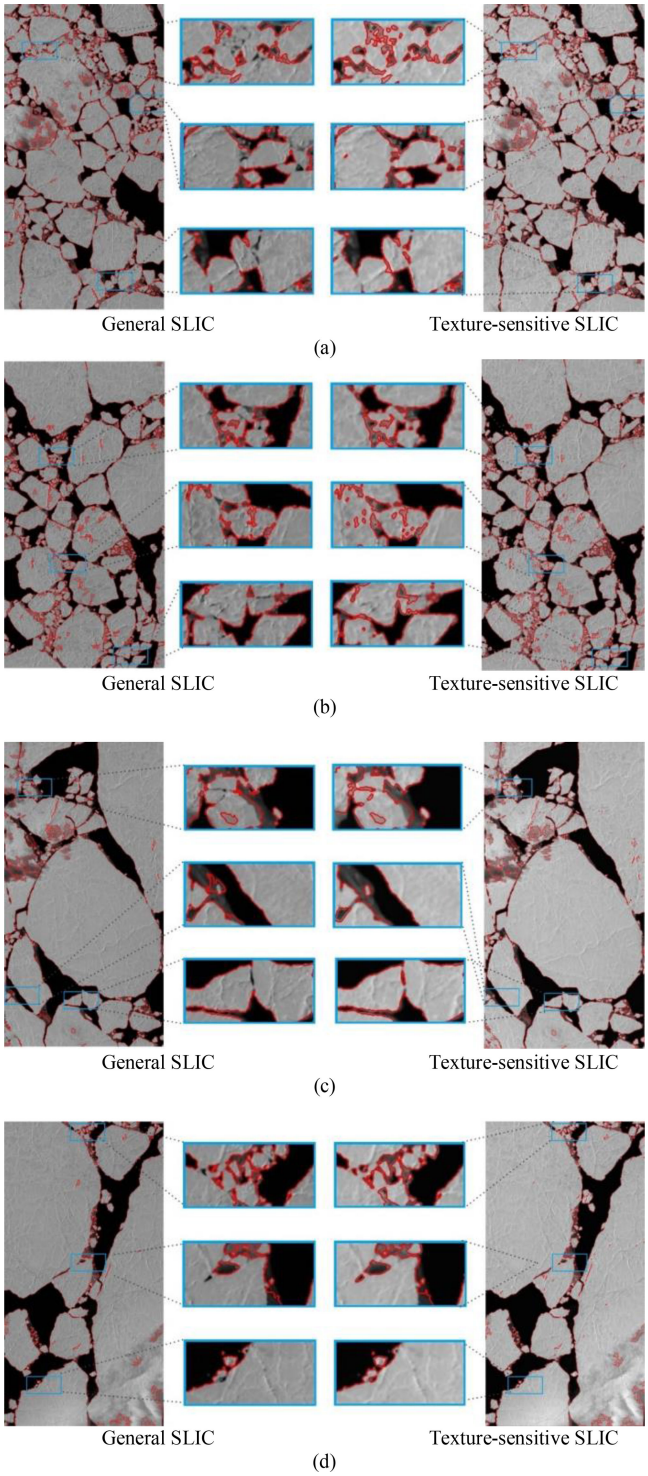

Fig. 6. Visual comparison of segmentation results. (a) Comparison of top-left image. (b) Comparison of top-right image. (c) Comparison of bottom-left image. (d) Comparison of bottom-right image.

We further compare visually our results with the method proposed in [27], which is a watershed with rule-based postprocessing, and the results are shown in Fig. 7. Although the method in [27] has a clear boundary, it has oversegmented large floes yet missing many small floes. This is possibly due to the fact that the watershed algorithm is an aggressive segmentation technique, which tends to generate oversegmented results. On the contrary, our method has almost no oversegmentation phenomenon, and the produced output fits the edge well.

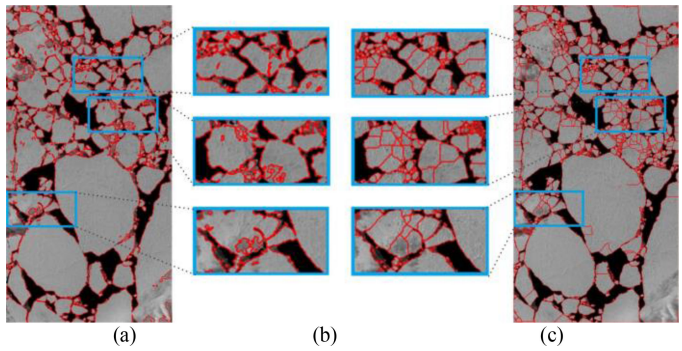

Fig. 7. Visual comparison of segmentation results. (a) Label output from our texture-sensitive SLIC algorithm. (b) Enlarged details comparison. (c) Label output from the method proposed in [26].

B. Algorithm Parameter Analysis

In SLIC, there are two important parameters that may affect its performance, i.e., the compactness factor m, which is set to 10 in this article, and the number of clusters k.

However, the selection of k varies with the type and resolution of the image. Luckily, based on abovementioned GT data and evaluation metrics, we can tune parameter k to achieve the best segmentation performance of the proposed algorithm. According to experience, too small k value will lead to poor segmentation performance and too large k will lead to large computation. For the test images, we tried different k values from 1000 to 12 000 in increments of 1000 superpixels to obtain statistics of evaluation metrics.

To further evaluate the effect of de-nosing based on RPCA, we compared the general SLIC method [(2) in Table II] and RPCA+ general SLIC method [(3) in Table II] with the proposed method [(4) in Table II]. The method (2) performed superpixels segmentation directlyta on the original sea ice image. And method (3) performed superpixels segmentation on the denoising image by using RPCA and bilateral filter. Fig. 8(a)–(c) shows the curves of ACC, F1 measure, and MCC with different k value using the general SLIC method, RPCA+ general SLIC method, and the proposed method, respectively. Fig. 8(d) shows the comprehensive comparison of ACC for three methods.

As can be seen from Fig. 8(a)–(c), the evaluation curves fluctuate as parameter k increases, and there is no obvious trend. But the changes of the three evaluation metrics are basically coordinated and can get the best performance at the same time. In Fig. 8(a) and (b), the general SLIC method and RPCA+ general SLIC method achieve the best performances when $k =$ 10 000. In Fig. 8(c), the proposed method achieves the best performances when $k = 6000$. Hence, it indicates that the selection of parameter k will affect the performance of the algorithm. Fig. 8(d) shows the comprehensive evaluation curves of three methods with different k. For the proposed method, a larger k

TABLE II
PERFORMANCE COMPARISON OF DIFFERENT SEGMENTATION ALGORITHMS

Methods	Acc (%)	Precision (%)	Recall (%)	F_1-measure (%)	MCC (%)	JAC (%)	Conformity (%)
(1) K-means + HMRF-EM	93.39	**99.37**	93.72	96.04	78.02	93.17	92.67
(2) General SLIC	95.00	98.74	95.41	97.23	81.14	94.61	94.31
(3) RPCA+ General	95.20	99.00	95.40	97.43	82.14	94.99	94.73
(4) Proposed method	**95.51**	99.00	**95.76**	**97.63**	**83.09**	**95.38**	**95.15**

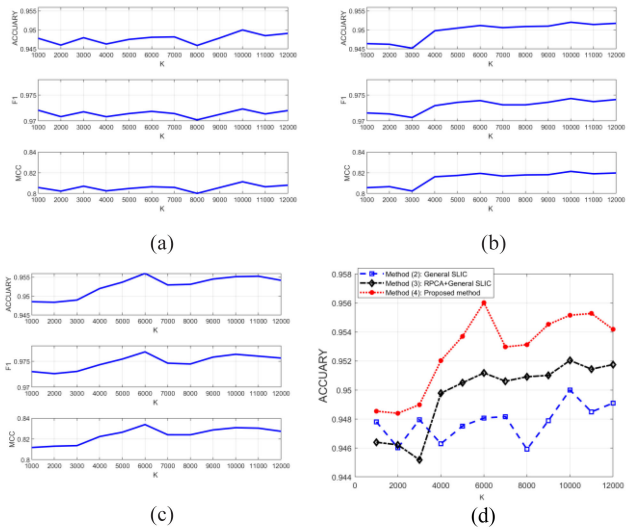

Fig. 8. Parameter k tuning using the evaluation metrics of three approaches. (a) General SLIC method. (b) RPCA+ General SLIC. (c) Proposed method. (d) Comparison of ACC.

makes it easier to achieve better performance and the ACC has a slight upward trend as the number of the superpixels increases. Meanwhile, it can be seen that the performance of the proposed method is better than the other two methods. At the same time, the performance of the RPCA+ general SLIC method is better than the general SLIC method. Hence, it can be concluded that denoising on low-rank sparse matrix is useful for removing noise in high-resolution optical images.

Although the value of k may affect the segmentation results, it is found that the variation of the results is quite small. When $k >= 4000$, the ACC is between 0.950 and 0.956. For simplicity, we set $k = 6000$; hence, the maximum number of pixels in each superpixel becomes $6368 \times 2584/6000 \approx 3000$ pixels. This seems to work well and hold a very steady performance, as validated in Fig. 8(d).

C. Quantitative Comparison

For quantitative performance comparison, the proposed method is benchmarked with the other three methods, including the abovementioned two superpixel-based segmentation methods and another segmentation method. Labeled as (1) in Table II, The third approach is based on the hidden Markov random field (HMRF) model and its expectation-maximization (EM) [29], which has been used for sea ice segmentation for its high ACC and robustness in image segmentation [30].

Table II describes the evaluation metrics computed from the proposed method and other state-of-the-art methods. For consistency of comparison and less computation, we use $k = 6000$ for all of the method (2)–(4). The proposed method (4) achieves the best ACC, Recall, F_1-measure, MCC, JAC, and Conformity of 95.51%, 95.76%, 97.63%, 83.09%, 95.38%, and 95.15%, respectively. The method (1) based on *K*-means and HMRF-EM obtains the best Precision of 99.37%, while the other metrics are quite poor. Overall these evaluation metrics show good consistency. Moreover, it can be seen that the de-noising method based on RPCA and texture-sensitive SLIC is useful to improve the segmentation performance.

The left column in Fig. 9 shows the original image, GT image, and segmentation results of abovementioned four methods. The right column of Fig. 9 shows the enlarged sections of them since the details are difficult to see clearly due to the high resolution of original image. The selected regions are shown in the box on the original images. As seen, method (1) can give a clearer boundary, yet it misses many small sea ice floes. Methods (2) and (3) can detect more small floes, yet they still miss some small ones. The result of method (3) is found to be better than that of method (2). It is consistent with the statistical data in Table II, which has validated that our proposed method can accurately segment the sea ice floes at different sizes with consistent boundaries.

In addition to visual comparison and quantitative evaluation, we also compare the histogram of segmentation results. With a bar plot for representing the distribution of numeric data into bins, histograms of the floe sizes can compare the results of floe size distribution (FSD). We compare the histograms of the GT image and segmentation results of the other four methods in Fig. 10. It can intuitively find that some small size of ices (especially about 10) are missed by method (1) and our proposed approach is better than methods (2) and (3).

The tested images have a spatial resolution of 1 m, and they are geocoded panchromatic images that cover an area of approximately 15×15 km. As seen in Fig. 10, the proposed method can accurately detect small ice floes under ten pixels. Actually, it can even detect ice floes as small as three pixels, which corresponds to a diameter of 3 m.

In order to compare histograms more accurately, we also used the Pearson correlation coefficient (PCC) to calculate the similarity between the two histograms as follows:

$$\mathrm{PCC}(H_1, H_2) = \frac{\sum_I (H_1(I) - \overline{H_1})(H_2(I) - \overline{H_2})}{\sqrt{\sum_I \left(H_1(I) - \overline{H_1}\right)^2 \sum_I \left(H_2(I) - \overline{H_2}\right)^2}} \tag{15}$$

where $\overline{H_k}$ is the mean value of H_k.

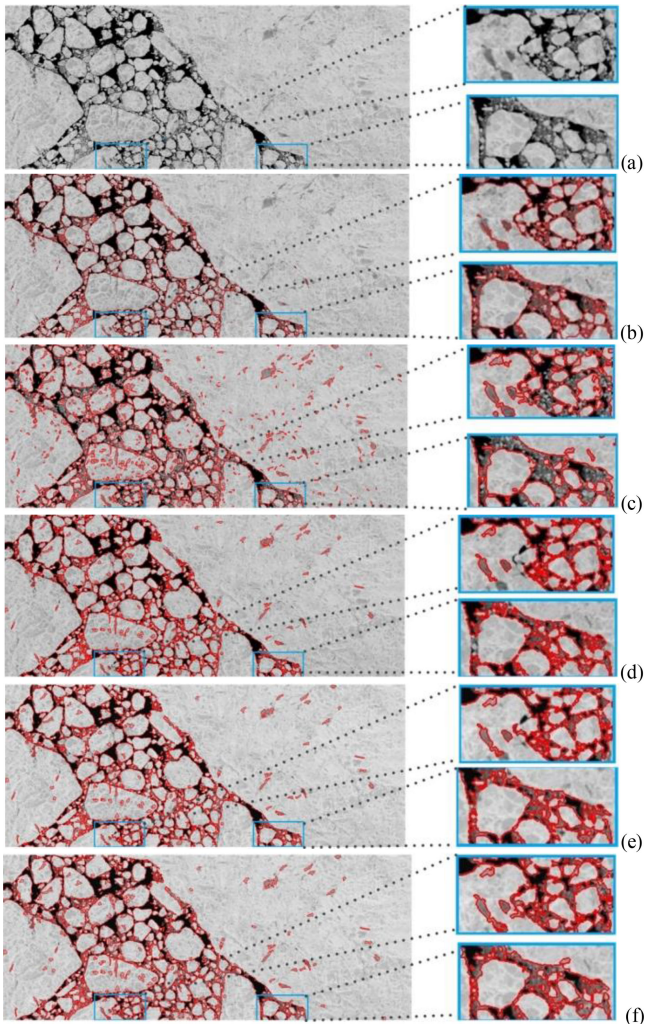

Fig. 9. Comparison of segmentation results with GT image. (a) Original sea ice image. (b) GT image. (c) Result of *K*-means + HMRF-EM. (d) Result of General SLIC. (e) Result of RPCA+ General SLIC. (f) Result of proposed method.

TABLE III
PERFORMANCE COMPARISON OF DIFFERENT ALGORITHMS

	OUR METHOD	RPCA+ GENERAL	K-MEANS + HMRF-EM
PCC	0.9136	0.9095	0.8448

The similarity between the derived histograms from the segmentation results in Fig. 10 and the GT are compared in Table III. As seen, the results are basically consistent with the visual comparison, which again have validated the superior performance of our proposed approach in segmentation of sea ice floes from HRO images.

D. Computational Time Comparison

To further evaluate the efficiency of the proposed algorithms, the running time of each stage of the algorithm is computed, respectively. We execute all experiments on a desktop computer with 16 GB RAM using MATLAB R2018a. The max number of iterations is set to 10 for the *K*-means + HMRF-EM segmentation method, and *k* is set to 6000 for the SLIC.

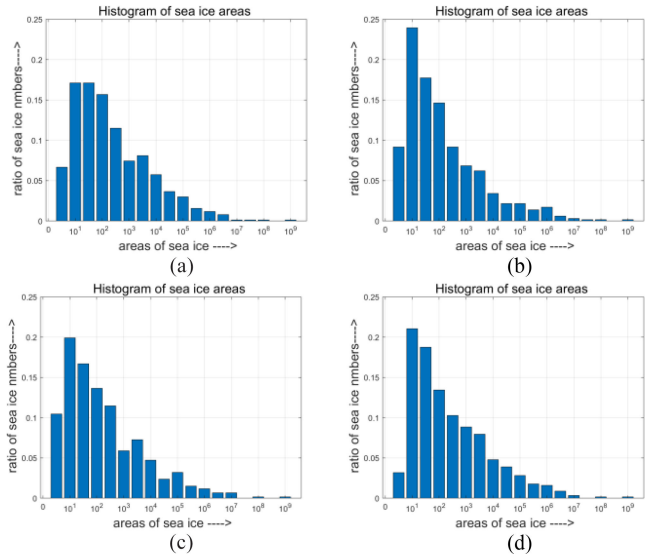

Fig. 10. Comparison the histograms of the derived sea ice segmentation results from (a) the ground truth, (b) our approach, (c) RPCA+ SLIC, and (d) *K*-means + HMRF-EM.

TABLE IV
RUNNING TIME OF DIFFERENT SEGMENTATION ALGORITHMS (IN SECONDS)

Methods	RPCA	SLIC	two-stage thresholding	Total
(1) K-means + HMRF-EM	/	/	/	2027.97
(2) General SLIC	/	226.33	310.23	536.56
(3) RPCA+ General	105.50	226.33	310.23	642.06
(4) Proposed method	105.50	307.64	310.23	723.37

As seen in Table IV, the SLIC-based methods are generally faster than the *K*-means + HMRF-EM method. While texture-sensitive SLIC takes 81.31s more than the general SLIC approach for computing the distance with LDZP. Moreover, de-noising takes about 105.5s and segmentation based on two-stage thresholding takes 310.23s. Therefore, postsegmentation of superpixels blocks need to be further improved and optimized in future work.

V. CONCLUSION

Automatic sea ice segmentation from high-resolution optical remote sensing images is a challenging task, due to the sea ices have wide spectral signature, texture, morphology, and size variability, especially when there is melting ice in the water. The use of low-rank sparse decomposition based on RPCA has successfully suppressed the noise in the images, which has been verified by experiments. To tackle the problem of high resolution and large image size, superpixel-based segmentation is found to be effective, especially with the improved texture-sensitive SLIC algorithm. The two-stage thresholding algorithm is also found to be very useful to generate the final segmentation. Quantitative and qualitative assessments have demonstrated the efficiency and efficacy of our proposed approach, which benefits from unsupervised analysis.

As future work, we will explore new models for improved denoising and segmentation, including kernel-based superpixles [32], 2-D singular spectral analysis based noise reduction [33], saliency detection [34], and folded-PCA-based dimension reduction [35]. By taking the segmentation results from conventional approaches as coarse GT, various deep learning models will also be explored, such as convolutional neural network in combination with multiscale spatial features [36], segmented stacked auto-encoders [37], combined loss learning [38], and optimized DenseNet [39]. Adaptive distancing-based unsupervised learning will also be explored [40]. Additional work will include extension of the algorithm for sea ice floe segmentation from other satellite images, such as SAR, and also possible fusion of different modalities for more accurate FSD analysis.

REFERENCES

[1] W. H. Lang, C. C. Chang, X. Z. Yang, J. Zhang, and J. M. Meng, "ScanSAR mode sea ice image segmentation," *Adv. Mater. Res.*, vol. 709, pp. 675–678, 2013.

[2] K. M. Stuart and D. G. Long, "Tracking large tabular icebergs using the SeaWinds Ku-band microwave scatterometers," *Deep Sea Res. Part II*, vol. 58, no. 11-12, pp. 1285–1300, 2011.

[3] F. Gao, X. Wang, Y. Gao, J. Dong, and S. Wang, "Sea ice change detection in SAR images based on convolutional-wavelet neural networks," *IEEE Geosci. Remote Sens. Lett.*, vol. 16 no. 8, pp. 1240–1244, Aug. 2019.

[4] Z. Shi, Z. Jiang, X. Yu, and B. Li, "Ship detection in high-resolution optical imagery based on anomaly detector and local shape feature," *IEEE Trans. Geosci. Remote Sens.*, vol. 52, no. 8, pp. 4511–4523, Aug. 2014.

[5] D. G. Barber and E. LeDrew, "SAR sea ice discrimination using texture statistics: A multivariate approach," *Photogrammetric Eng. Remote Sens.*, vol. 57, pp. 385–395, 1991.

[6] H. W. Deng and D. A. Clausi, "Unsupervised segmentation of synthetic aperture radar sea ice imagery using a novel Markov random field model," *IEEE Trans. Geosci. Remote Sens.*, vol. 43, no. 3, pp. 528–538, Mar. 2005.

[7] J. Ren, B. Hwang, P. Murray, S. Sakhalkar, and S. McCormack, "Effective SAR sea ice image segmentation and touch floe separation using a combined multi-stage approach," in *Proc. IEEE Int. Geosci. Remote Sens. Symp.*, 2015, pp. 1040–1043.

[8] D. A. Clausi and Q. Yu, "IRGS: Image segmentation using edge penalties and region growing," *IEEE Trans. Pattern Anal. Mach. Intell.*, vol. 30, no. 12, pp. 2126–2139, Dec. 2008.

[9] T. B. Ijitona, J. Ren, and P. B. Hwang, "SAR sea ice image segmentation using watershed with intensity-based region merging," in *Proc. IEEE 14th Int. Comput. Inf. Technol.*, 2014, pp. 168–172.

[10] C. Wang *et al.*, "Classification of the global Sentinel-1 SAR vignettes for ocean surface process studies," *Remote Sens. Environ.*, vol. 234, 2019, Art. no. 111457.

[11] P. Lu *et al.*, "Sea ice surface features in Arctic summer 2008: Aerial observations," *Remote Sens. Environ.*, vol. 114, no. 4, pp. 693–699, 2010.

[12] N. C. Wright and C. M. Polashenski, "Open-source algorithm for detecting sea ice surface features in high-resolution optical imagery," *Cryosphere*, vol. 12, no. 4, pp. 1307–1329, 2020.

[13] X. Miao, H. Xie, S. F. Ackley, and S. Zheng, "Object-based arctic sea ice ridge detection from high-spatial-resolution imagery," *IEEE Geosci. Remote Sens. Lett.*, vol. 13, no. 6, pp. 787–791, Jun. 2016.

[14] M. M. Barbat, C. Wesche, A. V. Werhli, and M. M. Mata, "An adaptive machine learning approach to improve automatic iceberg detection from SAR images," *Photogrammetry Remote Sens.*, vol. 156. no. 1, pp. 247–259, 2019.

[15] Z. Dong, M. Wang, D. Li, and Y. Cheng, "Optimal segmentation of high-resolution remote sensing image by combining superpixels with the minimum spanning tree," *IEEE Trans. Geosci. Remote Sens.*, vol. 56, no. 1, pp. 228–238, Jan. 2018.

[16] R. Achanta, A. Shaji, K. Smith, A. Lucchi, P. Fua, and S. Süsstrunk, "SLIC superpixels compared to state-of-the-art superpixel methods," *IEEE Trans. Pattern Anal. Mach. Intell.*, vol. 34, no. 11, pp. 2274–2281, Nov. 2012.

[17] G. Dong-Dong, T. Tang, Y. Li, and J. Lu, "Local pattern descriptor for SAR image classification," in *Proc. IEEE 5th Asia-Pacific Conf. Synthetic Aperture Radar*, Singapore, 2015, pp. 764–767.

[18] E. J. Candes, X. Li, Y. Ma, and J. Wright, "Robust principal component analysis?," *J. ACM*, vol. 58, no. 3, 2011, Art. no. 11.

[19] J. Wright, A. Ganesh, S. Rao, Y. Peng, and Y. Ma, "Robust principal component analysis: Exact recovery of corrupted low-rank matrices via convex optimization," in *Proc. 23rd Annu. Conf. Neural Inf. Process. Syst.*, 2009, pp. 2080–2088.

[20] S. Boyd *et al.*, "Distributed optimization and statistical learning via the alternating direction method of multipliers," *Found. Trends Mach. Learn.*, vol. 3, no. 1, pp. 1–122, 2011.

[21] S. Paris, J. Tumblin, P. Kornprobst, and F. Durand, "A gentle introduction to bilateral filtering and its applications," in *Proc. ACM SIGGRAPH*, 2007, pp. 1–50.

[22] Chukchi sea image source chukchi_20130531_2. 2013. [Online]. Available: https://lta.cr.usgs.gov/gfl/?img:3859:124&PTAGNAME=ArcticSea East Siberian Sea image source (esiber_20010616_1), 2001. https://lta.cr.usgs.gov/gfl/?img:672:125&PTAGNAME=ArcticSea

[23] S. K. Roy, B. Chanda, B. B. Chaudhuri, S. Banerjee, D. K. Ghosh, and S. R. Dubey, "Local directional ZigZag pattern: A rotation invariant descriptor for texture classification," *Pattern Recognit. Lett.*, vol. 108, pp. 23–30, 2018.

[24] LibSVM. 2019. [Online]. Available: https://www.csie.ntu.edu.tw/∼cjlin/libsvm/

[25] B. Hwang *et al.*, "Winter-to-summer transition of Arctic sea ice breakup and floe size distribution in the Beaufort Sea," *Elementa Sci. Anthropocene*, vol. 5, pp. 1–25, 2017.

[26] R. Kwok and N. Untersteiner, "New high-resolution images of summer Arctic sea ice," *EOS*, vol. 92, no. 7, pp. 53–54, 2011.

[27] B. Hwang *et al.*, "A practical algorithm for the retrieval of floe size distribution of Arctic sea ice from high-resolution satellite synthetic aperture radar imagery," *Elementa: Sci. Anthropocene*, vol. 5, pp. 1–23, 2017.

[28] H.-H. Chang, D. J. Valentino, A. H. Zhuang, and W.C. Chu, "Performance measure characterization for evaluating neuroimage segmentation algorithms," *Neuroimage*, vol. 47, no. 1, pp. 122–135, 2009.

[29] Q. Wang, "HMRF-EM-image: Implementation of the hidden Markov random field model and its expectation-maximization algorithm," 2012, *arXiv:1207.3510*.

[30] G. Akbarizadeh, Z. Tirandaz, and H. Kaabi, "PolSAR image segmentation based on feature extraction and data compression using weighted neighborhood filter bank and hidden Markov random field-expectation maximization," *Measurement*, vol. 153, 2020, Art. no. 107432.

[31] T. H. Ma, Z. Xu, and D. Meng, "Remote sensing image denoising via low-rank tensor approximation and robust noise modeling," *Remote Sens.*, vol. 12, 2020, Art. no. 1278.

[32] L. Fang, S. Li, W. Duan, J. Ren, and J. A. Benediktsson, "Classification of hyperspectral images by exploiting spectral–spatial information of superpixel via multiple kernels," *IEEE Trans. Geosci. Remote Sens.*, vol. 53, no. 12, pp. 6663–6674, Dec. 2015.

[33] J. Zabalza *et al.*, "Novel two-dimensional singular spectrum analysis for effective feature extraction and data classification in hyperspectral imaging," *IEEE Trans. Geosci. Remote Sens.*, vol. 53, no. 8, pp. 4418–4433, Aug. 2015.

[34] Y. Yan *et al.*, "Unsupervised image saliency detection with Gestalt-laws guided optimization and visual attention based refinement," *Pattern Recognit.*, vol. 79, pp. 65–78, 2018.

[35] J. Zabalza *et al.*, "Novel folded-PCA for improved feature extraction and data reduction with hyperspectral imaging and SAR in remote sensing," *ISPRS J. Photogrammetry Remote Sens.*, vol. 93, pp. 112–122, 2014.

[36] G. Sun *et al.*, "Deep fusion of localized spectral features and multi-scale spatial features for effective classification of hyperspectral images," *Int. J. Appl. Earth Observ. Geoinf.*, vol. 91, 2020, Art. no. 102157.

[37] J. Zabalza *et al.*, "Novel segmented stacked autoencoder for effective dimensionality reduction and feature extraction in hyperspectral imaging," *Neurocomputing*, vol. 185, pp. 1–10, 2016.

[38] Z. Fang *et al.*, "Triple loss for hard face detection," *Neurocomputing*, vol. 398, pp. 20–30, 2020.

[39] Z. Fang *et al.*, "Topological optimization of DenseNet with pretrained-weights inheritance and genetic channel selection," *Pattern Recognit.*, vol, 109, 2020, Art. no. 107608.

[40] H. Sun *et al.*, "Adaptive distance-based band hierarchy (ADBH) for effective hyperspectral band selection," *IEEE Trans. Cybern.*, in press, 2020, doi: 10.1109/TCYB.2020.2977750.

Yanmei Chai received the Ph.D. degree in computer science and technology from the Northwestern Polytechnical University (NWPU), Xi'an, China.

She is currently an Associate Professor with the Central University of Finance and Economics, Beijing, China. Her current research interests include image fusion, gait recognition, data analysis, and remote sensing.

Jinchang Ren (Senior Member, IEEE) received the B.Eng. degree in computer software, M.Eng. degree in image processing, and D.Eng. degree in computer vision from Northwestern Polytechnical University (NWPU), Xi'an, China, in 1992, 1997, and 2000, respectively, and the Ph.D. degree in media computing from the University of Bradford, Bradford, U.K., in 2009.

He is currently a Reader with the Department of Electronic and Electrical Engineering, University of Strathclyde, Glasgow, U.K. He has authored and coauthored more than 300 journal and conference papers. His research interests focus mainly on hyperspectral imaging, image processing, computer vision, big data analytics, and machine learning.

Prof. Ren is an Associate Editor for several international journals including the IEEE JOURNAL OF SELECTED TOPICS IN APPLIED EARTH OBSERVATIONS AND REMOTE SENSING and *Journal of The Franklin Institute*.

Byongjun Hwang (Member, IEEE) received the Ph.D. degree in microwave remote sensing from the University of Manitoba, Winnipeg, MB, Canada, in 2008.

He is currently a Reader with the Department of Biological and Geographical Sciences, School of Applied Sciences, University of Huddersfield, Huddersfield, U.K. As a Geophysicist and Remote Sensing Specialist, his research focuses on the dynamics and thermodynamics of snow and sea ice in the Arctic.

Jian Wang received the Ph.D. degree in signal and information processing from the Beijing University of Posts and Telecommunications, Beijing, China.

He is currently an Associate Professor with the Central University of Finance And Economics, Beijing, China. His research interests include machine learning, cloud computing, and intelligent education.

Dan Fan received the Ph.D. degree in computer science and technology from Tsinghua University, Beijing, China.

She is currently a Lecturer with the Central University of Finance and Economics, Beijing, China. Her research interests include data mining, pattern recognition, data analysis, adaptive modeling, and edge computing.

Yijun Yan received the B.E. degree in electrical engineering from the Shanghai University of Electric Power, Shanghai, China, in 2012, and the M.E. and Ph.D. degrees in electronic and electrical engineering from the University of Strathclyde, Glasgow, U.K., in 2013 and 2018, respectively.

He is currently a Research Associate with the Department of Electronic and Electrical Engineering, University of Strathclyde. His research interests include hyperspectral imaging, machine learning, image segmentation, and saliency detection.

Shiwei Zhu received the Ph.D. degree in management science and engineering from the Beihang University, Beijing, China, in 2011.

He is currently a Lecturer with the School of Information, Central University of Finance and Economics, Beijing, China. His research interests include data mining, management information system, and electronic commerce.